Optimal UAV-aided RFET System Design in Presence of Hovering Inaccuracy

Suraj Suman and Swades De

Abstract—In this paper, performance of unmanned aerial vehicle (UAV)-aided RF energy transfer (RFET) in presence of hovering inaccuracy is investigated. Hovering inaccuracy of UAV comprises of two types of mismatches: *Localization mismatch (LM)* and *Orientation mismatch (OM)*. Thus, a total of four combinations arise. Their impact on received power at ground deployed sensor node is characterized. For this purpose, a generalized radiation pattern of UAV-mounted transmitter antenna is considered. A closed-form expression of received power at the sensor node is obtained for each of these four cases. An optimization problem is formulated with the objective of optimizing the system parameters, such as transmit power, hovering altitude, and antenna exponent. This problem contains mixed nature of variables, i.e., continuous as well as discrete. To solve this problem, an algorithm, called *Hovering Inaccuracy-aware Optimal Charging System Design (HI-OCSD)*, is proposed to find the optimal system parameters. Through system simulations it is demonstrated that, hovering inaccuracy has notable impact on the performance, as received power at the sensor node reduces significantly in presence of hovering inaccuracy compared to ideal scenario. The effect of *LM* is more severe than that of *OM*. Further, a scenario with different level of hovering inaccuracy accounting for different deployment scenarios is considered, and the optimal system parameters are also evaluated. This study reveals that, UAV needs to hover at a relatively higher altitude to overcome the severity of hovering inaccuracy.

Index Terms—Unmanned aerial vehicle (UAV), wireless power transfer, radio frequency energy transfer, antenna radiation pattern, hovering inaccuracy, hovering altitude optimization

I. INTRODUCTION

In the upcoming era, Internet of Things (IoT) devices will monitor almost every phenomena around us. A few applications are unmanned security and defense, environmental sensing, health care, smart agriculture, and fire detection [1]. The IoT devices in such applications generate large volume of data (e.g., video, audio, image, text files) by sensing the surrounding, and this data is transmitted to the central entity (e.g., base station (BS)) for further decision making and automated action-ability [2], so that the undesired events can be detected and the assets are protected. For uninterrupted sensing and data gathering, the IoT devices need to operate perpetually. However, finite battery capacity of IoT devices is major hurdle towards this goal, as these devices consume significant amount of energy in sensing, processing, and communication [3].

The authors are with the Department of Electrical Engineering and Bharti School of Telecommunication, Indian Institute of Technology Delhi, New Delhi 110016, India (e-mail: {suraj.suman, swadesd}@ee.iitd.ac.in).

Battery replacement is not feasible in many applications due to its criticality or hard-to-reach deployment location. Also, this is not an environmental-friendly as well as cost-effective solution. In addition, wired power transmission infrastructure cannot be installed in these arduous locations due to physical, security or cost related constraints. To address the above issues, energy replenishment of low power IoT devices for sustainable operation is of high importance in the evolving 5G and beyond networking context.

A. State-of-the-Art

Energy harvesting from several environmental energy sources, such as solar [4], thermal [5], vibration [6], and ambient radio frequency (RF) [7] are powerful alternatives to replace or assist batteries of the IoT devices. The harvested energy extends the battery life significantly for low-power devices. Although these ambient energy sources are unlimited, they are not constantly available; even these sources may not be available at some inaccessible or interior locations. Therefore, ambient energy harvesting technologies do not ensure the perpetual operation of IoT devices in long run.

To overcome the randomness and availability issues of ambient sources, energy replenishment through dedicated energy source to the miniature wireless IoT nodes has been proposed in [8]. To this end, wireless power transfer (WPT) is a promising technology towards this, which offers on-demand energy supply delivery to the field nodes. This process is an effective solution especially in hard-to-reach deployment scenarios having no electricity infrastructure. Non-radiative and radiative wireless power transfer are two well-known methods for this [9]. Non-radiative wireless charging is based on coupling of magnetic field between coils of transmitter and receiver. However, this is not suitable in real-life deployment due to very short range operation. Also, it requires separate circuitry for data and energy transfer. In contrast, radiative power transfer offers more flexibility on alignment and leverages the advantage of beam steering over a large distance. Here, the RF waves can be used for carrying information as well as energy, and both are transferred using the same wave and same circuitry without additional radio hardware [10]. Off-the-shelf devices, such as Powercast energy harvester [11] can be easily embedded in the sensor nodes to facilitate RF energy transfer (RFET). In this work, RF energy transfer (RFET) technology is considered for WPT due to its advantages.

The static chargers equipped with WPT technology is used in [12] to maintain a certain power level in an area. This arrangement is expensive and requires installation of
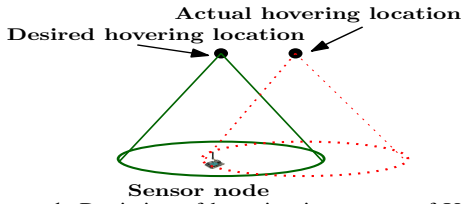
Figure 1: Depiction of hovering inaccuracy of UAV.

permanent infrastructure along with electric power supply provisioning for the fixed static chargers, which is not possible everywhere. To overcome this, the transmitter setup mounted on a ground based mobile vehicle (e.g., robot) is used, which arrives near the sensor node when required and replenishes energy wirelessly [13]–[15]. The terrestrial vehicles used for wireless recharging of sensor nodes are suitable in well-furnished environment , but not in other terrains, such as in agricultural and forest environments due to unavailability of physical path.

To address the issue of accessibility, unmanned aerial vehicle (UAV)-aided RFET has been proposed in [16]–[26]. In UAV-aided RFET, RF transmitter mounted on UAV arrives near the sensor nodes and charges them through RF radiation. The choice of UAV lies in its several properties, like excellent maneuverability, remote controllability, low cost, lightweight, and programming flexibility [27]. UAV can easily access hard-to-reach locations where human intervention is not feasible. Moreover, UAV-aided systems can be deployed within short time span to facilitate on-demand service. In view of the challenges of accessibility, fixed infrastructure deployment, and path availability, UAV has the capability to overcome these issues due to its mobility feature.

The works reported related to UAV-aided RFET can be categorized in three sets. In the first set of works, wireless charging of sensor nodes is of interest [16]–[21]. The time required to charge the sensor nodes was evaluated and different charging sequences are proposed in [16]. Here, the notion of RFET zone is conceptualized, and the sensor nodes lying inside it can harvest energy from the received signal from UAV-mounted transmitter. The trajectory of UAV in one dimension was studied in [17] aiming to maximize the energy transfer performance. This work was extended in two dimensional space for multiple sensor deployment scenario [18]. The solution obtained in these works [17], [18] are not global optimal, whereas the study in [19] presented the global optimal in one-dimensional space. Resource allocation (harvesting time, transmitted power level) problem for UAV-assisted networks was investigated in [20], where UAV acts as an energy source to power multiple energy harvesting-enabled device-to-device pairs. A wireless charging platform integrated with a quadcopter was presented in [21] to provide desirable energy for sensing applications.

In the second set of works, energy transfer as well as information transfer are of interest [22]–[24]. The WPT and data collection framework was presented in [22], where Markov Decision Process is used to formulate the problem and solved using Q-learning. On the other hand, UAV-assisted simultaneous wireless information and power transfer was studied in

[23], where average data rate requirement of each IoT device is guaranteed from the energy harvested from the received signal from the transmitter mounted on UAV. In [24], the transmission capability of UAV was powered by radio signal transmitted by the source via time-sharing mechanism.

In the third set, wireless charging along with mobile edge computing framework were explored to prolong the lifetime of sensor nodes [25], [26]. The data of sensor nodes is offloaded to the edge servers mounted on UAV lying in its vicinity, to perform heavy computation tasks. This reduces the burden on low power IoT devices and prolongs the lifetime of sensor nodes. UAV-enabled edge computing wireless-powered system was studied in [25], where the resources, like computation, bandwidth, harvesting time, are allocated along with UAV trajectory optimization.

B. Motivation and Contributions

In the reported works related to UAV-aided RFET, perfect hovering condition of UAV has been considered, which is not the case in real-life deployment scenario. In a recent study in [28], the hovering inaccuracy of UAV has been measured and quantified through extensive experiments. Hovering inaccuracy of UAV refers to the error during the execution of mission due to imperfect hovering. This is depicted in Fig. 1, where UAV hovers at a slightly different location other than desired position, and vibrates at this point rather than being stationary. The operating condition of UAV-aided system is very different from fixed deployed static systems, because UAV has to hover in the sky in three-dimensional space while carrying some payload. The hovering condition of UAV strongly depends upon the deployment scenario and surrounding environment. Deployment scenario refers to number of available satellites and multipath propagation, whereas surrounding environment refers to wind speed, smog, weather condition.

While the experimental study in [28] modeled the UAV hovering inaccuracy, performance deviation of RFET was not quantified. To this end, the study in this work focuses on UAV-aided RFET performance quantification, wherein the impact of individual as well as joint mismatches are characterized in order to identify the severity of each mismatch.

The impact of hovering inaccuracy is not severe in UAV-aided cellular communication, due to higher operational altitude along with much lower receive power-threshold for information transfer is about -100 dBm [29]. On the contrary, the receive power threshold in energy transfer is about -12 dBm. Due to sensitivity difference, the range of RFET is limited to very small distance (up to a few meters) compared to the range of wireless information transfer (up to a few kilometers). Therefore, inclusion of hovering inaccuracy is important in UAV-aided RFET system design. Without accounting this factor, the system is expected to experience under-provisioning of resource. The focus of this work is on energy transfer application only, because the receiver sensitivity is significantly more stringent for energy transfer as compared to information transfer.

The key contributions and significance of this work are as follows:

- Hovering inaccuracy of UAV is considered in the system model for analysis. Hovering inaccuracy comprises of two types of mismatches: *Localization mismatch (LM)* and *Orientation mismatch (OM)*, and thus a total of four combinations arise. Closed-form expressions for the received power in each case are obtained for a generalized radiation pattern of antenna, and their natures are characterized.

- An optimization problem is formulated to estimate the optimal system parameters (transmit power, hovering altitude of UAV, antenna exponent), which contains mixed type of variables (continuous as well as discrete). The expression of received power is quite different for even and odd numbers in all the four cases, which discourages to use integer relaxation method. In order to solve this problem, an algorithm, called *Hovering Inaccuracy-aware Optimal Charging System Design (HI-OCSD)*, is proposed to obtain the optimal system parameters.

- The simulation results reveal that, hovering inaccuracy has notable impact on performance. It requires to transmit high power level to achieve the same performance in presence of hovering inaccuracy as compared to the ideal scenario, i.e., without any hovering inaccuracy. In addition, *LM* dominates the hovering inaccuracy compared to *OM*.

- A framework to analyze different level of hovering inaccuracy accounting different deployment area is presented. A tuning parameter is used for this purpose, which indicates the severity of hovering inaccuracy. The performance studies indicate that, UAV needs to increase its altitude to overcome the effect of hovering inaccuracy. The hovering condition of UAV has remarkable effect on the optimal system design during UAV-aided RFET.

The study in this paper is important in accurately quantifying the overhead in UAV-aided RFET as a function of hovering inaccuracy. It also provides insights on devising communication technology solutions to overcome hovering inaccuracy, thereby enhancing the performance.

C. Paper Organization

The paper is organized as follows. In Section II, hovering inaccuracy is briefly discussed and system model for UAV-aided RFET is presented. Hovering inaccuracy is characterized in Section III. An optimization problem to estimate the optimal system parameters is formulated in Section IV. Simulation results are discussed in Section V. Performance for different level of hovering inaccuracy is investigated in Section VI, followed by concluding remarks in Section VII.

II. Hovering Inaccuracy of UAV and System Model

A. Hovering Inaccuracy of UAV

The locations of field nodes to be charged along with hovering altitude are fetched into the UAV from ground control station in order to facilitate UAV-aided RFET. It is desired that, UAV hovers just above the sensor node at an optimum altitude and remains stationary while facilitating RFET, such that maximum power can be transferred at the ground sensor node. The distance between transmitter and receiver is minimum in this orientation, and the center of beam spot of transmitter antenna points towards the field sensor node. But, this does not happen in practical deployment scenario due to hovering inaccuracy of UAV. It may be noted that, the gain of transmitter antenna is maximum at the center of the beam in case of directional antenna. Hovering inaccuracy mainly comprises two types of mismatches: *LM* and *OM*.

LM is caused by positioning error from the global positioning system (GPS), wherein the UAV hovers at a little different location other than the desired one (see Fig. 1). This leads to change in distance as well as elevation angle between transmitter and receiver. $d(h)$ and $\Phi_{LM}(h)$ respectively denote the distance and elevation angle due to *LM* when UAV hovers at altitude h.

In addition to this, UAV undergoes rotation at the hovering location, which is responsible for *OM*. There are three types of rotational motion: *pitch*, *roll*, and *yaw*. *Pitch* corresponds to rotation around the lateral axis or around the wings, *roll* corresponds to rotation around the longitudinal axis or around the head, whereas *yaw* corresponds to rotation around the vertical plane. Due to rotation, the center of beam spot of the transmitter antenna mounted on UAV is displaced and does not point towards the receiver antenna. This rotation is responsible for change in elevation angle between transmitter and receiver. The distance between transmitter and receiver does not change due to *OM*, whereas the distance remains same as hovering altitude. The elevation angle caused by *OM*, when UAV hovers at altitude h, is denoted as $\Phi_{OM}(h)$.

By including the effect of both mismatches (i.e., *LM* and *OM*), the distance as well as elevation angle between transmitter and receiver are altered from the ideal ones. However, the distance between transmitter and receiver is the same as that in case of *LM*, whereas elevation angle is different from those in case of *LM* and *OM*. The elevation angle between transmitter and receiver in presence of both mismatches, when UAV hovers at altitude h, is denoted as $\Theta(h)$.

These mismatches were measured using extensive field experiments using a rotatory-wing UAV. The GPS location of the sensor node placed at ground and altitude of operation were fed into the Ardupilot mission planner (http://ardupilot.org), which was installed in the computer acting as ground control station. The UAV setup hovers at different altitude for approximately three minutes at each altitude above the ground sensor node. The data of GPS location and rotational motion parameter of UAV, i.e., pitch, roll, and yaw, were collected. This data was analyzed and the variation of hovering inaccuracy parameter was captured using curve fitting technique for further analysis. The detailed discussion on hovering inaccuracy is not included here for brevity, which can be found in [28]. The variation of different parameters (distance and elevation angle) caused by different mismatches are listed in Table I, which are used in this work. $\mathcal{N}$ denotes a Gaussian random variable. It may be noted that, $0 \leq \Phi_{LM}(h), \Phi_{OM}(h), \Theta(h) < \pi/2$, and the bound on elevation angle $\Theta(h)$ is given as [28]:

$$\Phi_{LM}(h) - \Phi_{OM}(h) \leq \Theta(h) \leq \Phi_{LM}(h) + \Phi_{OM}(h). \quad (1)$$
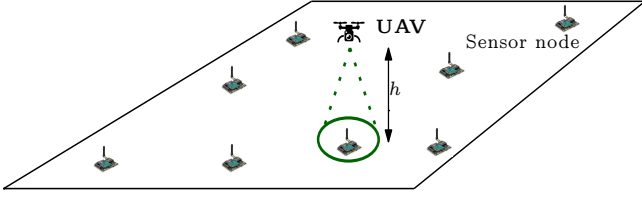
Figure 2: System model for UAV-aided RFET.

B. System Model

The system model for charging of sensor nodes in real-life practical deployment scenario is shown in Fig. 2, where a UAV charges the sensor nodes by hovering above each of them. After charging a node the UAV moves to the other energy-depleted sensor nodes to facilitate UAV-aided RFET to the field nodes. In this way, a UAV can attend several field deployed sensor nodes in sequential manner. The analysis as well as the consequences of hovering inaccuracy for charging the other sensor nodes remain the same during their respective turns of charging. Therefore, in this work without loss of generality we restrict our analysis for a single sensor node.

UAV charges the sensor nodes individually by hovering just above each of them through a one-on-one link, which is practically feasible due to several peculiarities of UAV-aided RFET. The distance between transmitter and receiver as well as the effect of shadow fading is minimum when UAV hovers just above the target sensor node [30], which offers maximum energy transfer over a given time. Path loss as well as shadow fading increase when the UAV hovers at different location other than just above the individual sensor nodes. This leads to reduction in received power, and hence a reduced harvested power. Thus, charging a group of sensor nodes simultaneously in a clustered fashion in RFET application is not efficient. Further, the previous studies reported in [18], [31] also suggest that, the scheme of UAV hovering just above the individual sensor nodes converges towards optimal when the duration of operation is longer. This is the scenario in the given context of UAV-aided RFET, where UAV has to hover for appreciably long time duration, up to several minutes, to replenish sufficient amount of energy (up to a few Joules) to each of the sensor nodes. Therefore, one-to-one link is preferred, to ensure a higher energy transfer.

Besides this, the use of directional antenna having limited ground coverage area necessitates that the sensor nodes are charged individually. Moreover, compared to the limited RFET range the separation between deployed field nodes is sufficiently large in real-life deployment scenario. These practical considerations also suggest to charge the sensor nodes individually by establishing a one-on-one link.

The target sensor node experiences the effect of UAV hovering inaccuracy during its charging. By considering the effect of hovering inaccuracy, the power received at a sensor node when the UAV hovers at altitude h is expressed as:

$$P^{rx}(h, n, \theta) = P_{tx} \cdot G_{rx} \cdot g(n, \theta) \cdot \left(\frac{\lambda}{4\pi d_{tx-rx}} \right)^2$$
$$= P_{tx} \cdot G_0 \cdot g(n, \theta) \cdot \left(\frac{1}{d_{tx-rx}} \right)^2 \tag{2}$$

where P_{tx} is the power transmitted by transmitter mounted on UAV and G_{rx} is the receiver antenna gain. The receiver antenna is omnidirectional, which is capable of receiving signals from all directions. λ is the wavelength of transmitted RF wave with $G_0 = G_{rx} \cdot \left(\lambda/4\pi \right)^2$. d_{tx-rx} is distance between transmitter and receiver, which depends on the UAV hovering altitude. $g(n, \theta)$ is the generalized radiation pattern of transmitter antenna mounted on the bottom of UAV. It is given as [32]:

$$g(n, \theta) = 2 \cdot (n + 1) \cdot \cos^n(\theta), \tag{3}$$

where n is antenna exponent, and θ denotes the elevation angle between transmitter and receiver. The main lobe of this antenna mounted on UAV points down towards the ground deployed sensor node as shown in Fig. 2. The beam width θ_{HPBW} of this radiating antenna is:

$$\theta_{HPBW} = \sqrt{\frac{4\pi}{2(n+1)}}. \tag{4}$$

It may be noted that, the received power obtained in (2) depends on the transmitted power, transmitter antenna gain, and transmitter to receiver distance. Further, radiation profile of the transmitter antenna depends on the antenna exponent n and elevation angle θ between the transmitter and the receiver. The hovering inaccuracy leads to change in θ and transmitter-to-receiver distance, which is a function of h (see Table I), and hence the field deployed sensor node experiences the effect of hovering inaccuracy in UAV-aided RFET.

For analytical tractability, the value of antenna exponent n is considered integer values. The characteristics for real numbers lie in between the integer values, and hence this assumption will not affect the analysis. Thus, $\cos^n \theta$ is written as follows:

$$\cos^n \theta = \begin{cases} \frac{1}{2^{n-1}} \left[\sum\limits_{r=0}^{\frac{n}{2}-1} \binom{n}{r} \cos((n-2r)\theta) \right] \\ + \frac{1}{2^n} \binom{n}{n/2}, & \text{if } n = \text{even} \\ \frac{1}{2^{n-1}} \left[\sum\limits_{r=0}^{\frac{n-1}{2}} \binom{n}{r} \cos((n-2r)\theta) \right], & \text{if } n = \text{odd}. \end{cases} \tag{5}$$

Remark 1. *The emphasis of the study is to analyze the impact of hovering inaccuracy on performance, and received power is considered as performance metrics due to its analytical tractability. Since the harvested power is non-decreasing function of the received power, the analysis on received power will remain valid for computing harvested power [18], [19]. Further, the harvested or transferred energy to the sensor node, which is the product of harvested power and charging time, will also depend upon the received power level.*

Remark 2. *Fading is not taken into consideration in the*

Table I: Variation of different parameters of hovering inaccuracy.

Localization mismatch	$d(h) = \sqrt{u_1 h^2 + u_2 h + u_3}$; $u_1 = 1.015, u_2 = -0.1193, u_3 = 0.2588$, $\Phi_{LM}(h) = v_1 h^3 + v_2 h^2 + v_3 h + v_4$; $v_1 = -0.01573, v_2 = 0.1763, v_3 = -0.651, v_4 = 0.8488$.
Orientation mismatch	$d(h) = h$ $\Phi_{OM}(h) \sim \mathcal{N}\big(\mu_{OM}(h), \sigma^2_{OM}(h)\big)$, $\mu_{OM}(h) = w_1 h^3 + w_2 h^2 + w_3 h + w_4$; $w_1 = 0.00125, w_2 = -0.01073, w_3 = 0.01871, w_4 = 0.0623$ $\sigma_{OM}(h) = z_1 h^3 + z_2 h^2 + z_3 h + z_4$; $z_1 = -0.001128, z_2 = 0.009966, z_3 = -0.03044, z_4 = 0.06542$.
Both mismatch	$d(h) = \sqrt{u_1 h^2 + u_2 h + u_3}$; $u_1 = 1.015, u_2 = -0.1193, u_3 = 0.2588$, $\Theta(h) \sim \mathcal{N}\big(\mu_M(h), \sigma^2_M(h)\big)$, $\mu_M(h) = a_1 h^3 + a_2 h^2 + a_3 h + a_4$; $a_1 = -0.01371, a_2 = 0.1518, a_3 = -0.5653, a_4 = 0.7925$, $\sigma_M(h) = b_1 h^3 + b_2 h^2 + b_3 h + b_4$; $b_1 = -0.000584, b_2 = 0.00523, b_3 = -0.0209, b_4 = 0.06973$.

analysis. RFET operation is facilitated over a longer time duration (up to a few minutes) to charge the sensor nodes [16], which averages out the multipath fading. Also, the use of directional antenna overcomes the effect of multipath fading by focusing the RF energy transmission in a particular direction.

Remark 3. *The use of directional antenna has several benefits, such as relatively higher received power due to higher gain, fading mitigation, and relatively higher coverage along line-of-sight (LoS). Due to this, free space path loss model is precisely accurate for analysis and system design in case of directional antenna usage. On the other hand, deployment-specific generalized path loss model is required in case of omnidirectional antenna, as different deployment scenarios have different characteristics in terms of channel model or path loss. For example, deployment scenarios in suburban, urban, and agriculture have different fading parameters [30].*

III. CHARACTERIZATION OF HOVERING INACCURACY

As noted in Section II, the distance as well as elevation angle between transmitter (mounted on UAV) and receiver (field sensor node on ground) changes due to hovering inaccuracy of UAV. Moreover, the received power at the ground sensor node depends upon the distance as well as elevation angle along with the type of antenna used. In this section, the individual as well as joint impact of mismatches on the performance, a total of four cases, are characterized. This study assesses the deviation in performance compared to ideal scenario along with identifying the severity of each mismatch.

A. No Hovering Inaccuracy (Ideal)

When the UAV hovers just above the sensor node and does not undergo rotation at this location, the ground sensor node does not experience any hovering inaccuracy (*LM* or *OM*). Hence, from (2), the received power at the sensor node is obtained as,

$$
\begin{aligned}
P_{rx}^{(1)}(h, n) &= P_{tx}^{(1)} \cdot G_0 \cdot g(n, \theta) \cdot \left(\frac{1}{d_{tx-rx}}\right)^2 \Bigg|_{\substack{\theta = 0, \\ d_{tx-rx} = h}} \\
&= P_{tx}^{(1)} \cdot G_0 \cdot 2(n+1) \cdot \frac{1}{h^2} \\
&= P_{tx}^{(1)} \cdot G_0 \cdot W_1(h, n)
\end{aligned}
$$
(6)

where $P_{tx}^{(1)}$ is the power transmitted by transmitter mounted on UAV in ideal scenario. $W_1(h, n)$ is defined as,

$$
W_1(h, n) = 2(n+1) \cdot \frac{1}{h^2}.
$$
(7)

One can observe from (6) that, the distance between transmitter and receiver d_{tx-rx} is the same as hovering altitude h due to the absence of *LM*. Further, the elevation angle θ between transmitter and receiver is 0, because there is neither *LM* nor *OM*, and the antenna beam points towards the sensor node.

It may be noted that, $W_1(h, n)$ is an increasing function of antenna exponent for a given hovering altitude. In addition, $W_1(h, n)$ is a decreasing function of hovering altitude for a given antenna exponent.

B. With Only Localization Mismatch (LM)

In this case, ground projection point of the hovering UAV is a little different from the desired position, but the UAV does not undergo rotation. Thus, the ground sensor node experiences only *LM*. This leads to change in distance as well as elevation angle between transmitter and receiver (see Table I). Hence, from (2), the received power at the sensor node is obtained as,

$$
\begin{aligned}
P_{rx}^{(2)}(h, n) &= P_{tx}^{(2)} \cdot G_0 \cdot g(n, \theta) \cdot \left(\frac{1}{d_{tx-rx}}\right)^2 \Bigg|_{\substack{\theta = \Phi_{LM}(h), \\ d_{tx-rx} = d(h)}} \\
&= P_{tx}^{(2)} \cdot G_0 \cdot 2(n+1) \cdot \cos^n(\Phi_{LM}(h)) \cdot \frac{1}{d^2(h)} \\
&= P_{tx}^{(2)} \cdot G_0 \cdot W_2(h, n)
\end{aligned}
$$
(8)

where $P_{tx}^{(2)}$ is the power transmitted by UAV-mounted transmitter with *LM*-only. $W_2(h, n)$ is defined as,

$$
W_2(h, n) = 2(n+1) \cdot \cos^n(\Phi_{LM}(h)) \cdot \frac{1}{d^2(h)}.
$$
(9)

The effect of LM-only is noted from (8), wherein the distance between transmitter and receiver d_{tx-rx} is $d(h)$, given in Table I, rather than the hovering altitude of UAV as in case of ideal scenario. Besides, the elevation angle $\theta = \Phi_{LM}(h)$ between transmitter and receiver is non-zero, given in Table I.

Lemma 1. $W_2(h, n)$ *is a unimodal function of hovering altitude h, for a given antenna exponent $n = n_0$.*

Proof: See Appendix A. ■

Lemma 2. $W_2(h, n)$ *is a unimodal function of antenna exponent n, for a given hovering altitude $h = h_0$.*

Proof: See Appendix B. ■

C. With Only Orientation Mismatch (OM)

In this case, UAV is considered to hover above the desired ground position, but it undergoes rotation at this location. Thus, the ground sensor node experiences only *OM*, which leads to change in only elevation angle (see Table I). This leads to change in elevation angle between transmitter and receiver; distance does not change. Hence, from (2), the received power at the sensor node is obtained as,

$$P_3(h, n, \theta) = P_{tx}^{(3)} \cdot G_0 \cdot g(n, \theta) \cdot \left(\frac{1}{d_{tx-rx}} \right)^2 \Big|_{\substack{\theta = \Phi_{OM}(h), \\ d_{tx-rx} = h}}$$

(10)

where $P_{tx}^{(3)}$ is the power transmitted by UAV-mounted transmitter with *OM*-only.

It can be noted from Table I that the elevation angle $\Phi_{OM}(h)$ is a Gaussian random variable. The mean and standard deviation of this distribution vary with hovering altitude h. The received power in expected sense is a correct metric for performance evaluation, as UAV has to hover for long time duration (up to a few minutes) in the given context of RFET. Hence, the received power in expected sense is expressed as:

$$
\begin{aligned}
P_{rx}^{(3)}(h, n) &= \mathbb{E}\big[P_3(h, n, \theta)\big] \\
&= \int_{-\infty}^{\infty} P_{tx}^{(3)} \cdot G_0 \cdot g(n, \theta) \cdot \left(\frac{1}{h} \right)^2 \cdot f_{\Phi_{OM}(h)}(\theta) \cdot d\theta \\
&= P_{tx}^{(3)} \cdot G_0 \cdot \left(\frac{1}{h} \right)^2 \int_{-\infty}^{\infty} g(n, \theta) \cdot f_{\Phi_{OM}(h)}(\theta) \cdot d\theta
\end{aligned}
$$

(11)

Remark 4. *If $\mathcal{X}$ is a Gaussian random variable with mean $\mu_\mathcal{X}$ and standard deviation $\sigma_\mathcal{X}$, then its characteristic function $\Psi_\mathcal{X}(\tau)$ is given as:* $\Psi_\mathcal{X}(\tau) = \mathbb{E}[\exp(i\tau\mathcal{X})] = \exp(i\tau\mu_\mathcal{X} - \frac{1}{2}\sigma_\mathcal{X}^2 \tau^2)$, *where i denotes the imaginary number. Then, the following expression can be written using this characteristics function:*

$$\mathbb{E}[\cos(\tau\mathcal{X})] = \cos(\mu_\mathcal{X}\tau) \cdot \exp(-\frac{1}{2}\sigma_\mathcal{X}^2\tau^2). \quad (12)$$

Using the finding in (12), (11) is rewritten as:

$$
\begin{aligned}
P_{rx}^{(3)}(h, n) &= P_{tx}^{(3)} \cdot G_0 \cdot \left(\frac{1}{h} \right)^2 \int_{-\infty}^{\infty} g(n, \theta) \cdot f_{\Phi_{OM}}(\theta) \cdot d\theta \\
&= P_{tx}^{(3)} \cdot G_0 \cdot W_3(h, n)
\end{aligned}
$$

(13)

where $W_3(h, n)$ is defined as:

$$W_3(h, n) = \frac{1}{h^2} \cdot \begin{cases} X_{even}(h, n), & \text{if } n = \text{even} \\ X_{odd}(h, n), & \text{if } n = \text{odd} \end{cases} \quad (14)$$

with $\qquad X_{even}(h, n) \qquad = \qquad \frac{1}{2^{n-1}}\Big[\sum_{r=0}^{\frac{n}{2}-1} \binom{n}{r} \cos((n \quad -$

$2r)\mu_{OM}(h)) \exp\big(-\tfrac{1}{2}(n-2r)^2\sigma_{OM}^2(h)\big)\Big] + \frac{1}{2^n}\binom{n}{n/2}$

and $\qquad X_{odd}(h, n) \qquad = \qquad \frac{1}{2^{n-1}}\Big[\sum_{r=0}^{\frac{n-1}{2}} \binom{n}{r} \cos((n \quad -$

$2r)\mu_{OM}(h)) \exp\big(-\tfrac{1}{2}(n-2r)^2\sigma_{OM}^2(h)\big)\Big].$

Lemma 3. $W_3(h, n)$ *is a non-increasing function of hovering altitude h, for a given antenna exponent $n = n_0$.*

Proof: See Appendix C. ■

Lemma 4. $W_3(h, n)$ *is a non-decreasing function of antenna exponent n, for a given hovering altitude $h = h_0$.*

Proof: See Appendix D. ■

D. With Both LM and OM

When UAV does not hover above the desired ground position and also undergoes rotation; the ground sensor node experiences both *LM* and *OM*. This leads to change in elevation angle as well as distance between transmitter and receiver (see Table I). Accordingly, the received power at the sensor node is obtained as,

$$P_4(h, n, \theta) = P_{tx}^{(4)} \cdot G_0 \cdot g(n, \theta) \cdot \left(\frac{1}{d_{tx-rx}} \right)^2 \Big|_{\substack{\theta = \Theta(h), \\ d_{tx-rx} = d(h)}}$$

(15)

where $P_{tx}^{(4)}$ is the power transmitted by UAV-mounted transmitter with both *LM* and *OM*.

As mentioned in Table I, the elevation angle is a random variable, which follows Gaussian distribution. The mean and standard deviation of this distribution vary along hovering altitude. Hence, the received power in expected sense is given as,

$$
\begin{aligned}
P_{rx}^{(4)}(h, n) &= \mathbb{E}\big[P_4(h, n, \theta)\big] \\
&= \int_{-\infty}^{\infty} P_{tx}^{(4)} \cdot G_0 \cdot g(n, \theta) \cdot \left(\frac{1}{d(h)} \right)^2 \cdot f_{\Theta(h)}(\theta) \cdot d\theta \\
&= P_{tx}^{(4)} \cdot G_0 \cdot \left(\frac{1}{d(h)} \right)^2 \int_{-\infty}^{\infty} g(\theta) \cdot f_{\Theta(h)}(\theta) \cdot d\theta.
\end{aligned}
$$

(16)

Using the finding in (12), (16) is rewritten as,

$$
\begin{aligned}
P_{rx}^{(4)}(h, n) &= P_{tx}^{(4)} \cdot G_0 \cdot \left(\frac{1}{d(h)} \right)^2 \int_{-\infty}^{\infty} g(n, \theta) \cdot f_\Theta(\theta) \cdot d\theta \\
&= P_{tx}^{(4)} \cdot G_0 \cdot W_4(h, n)
\end{aligned}
$$

(17)

where $W_4(h, n)$ is defined as,

$$W_4(h, n) = \frac{1}{d^2(h)} \cdot \begin{cases} Y_{even}(h, n), & \text{if } n = \text{even} \\ Y_{odd}(h, n), & \text{if } n = \text{odd} \end{cases} \quad (18)$$

with $\qquad Y_{even}(h, n) \qquad = \qquad \frac{1}{2^{n-1}}\Big[\sum_{r=0}^{\frac{n}{2}-1} \binom{n}{r} \cos((n \quad -$

$2r)\mu_M(h)) \exp\big(-\tfrac{1}{2}(n-2r)^2\sigma_M^2(h)\big)\Big] + \frac{1}{2^n}\binom{n}{n/2}$

and $Y_{odd}(h,n) = \frac{1}{2^{n-1}} \Big[\sum_{r=0}^{\frac{n-1}{2}} \binom{n}{r} \cos((n-2r)\mu_M(h)) \exp\big(-\frac{1}{2}(n-2r)^2\sigma_M^2(h)\big) \Big]$.

Lemma 5. *$W_4(h,n)$ is a unimodal function of hovering altitude h, for a given antenna exponent $n = n_0$.*

Proof: See Appendix E. ∎

Lemma 6. *$W_4(h,n)$ is a unimodal function of antenna exponent n, for a given hovering altitude $h = h_0$.*

Proof: See Appendix F. ∎

Remark 5. *The presented analysis remains valid also for omnidirectional antenna, which corresponds to $n = 0$. Hence, from (2), the received power $P_{rx}^{(omni)}(h,n)$ is found as,*

$$P_{rx}^{(omni)}(h, n=0) = P_{tx}^{(omni)} \cdot G_0 \cdot \frac{2}{d^2(h)}. \quad (19)$$

The ground sensor node experiences only LM. It does not experience OM due to large beam width of omnidirectional antenna, which has sufficient projection area on the ground to cover the sensor node.

IV. SELECTION OF OPTIMAL SYSTEM PARAMETER

With the characterization of hovering inaccuracy in the previous section, it is important to select the system parameters, such as transmit power, hovering altitude, and antenna exponent in order to maximize the received power at the ground sensor node in order to transfer higher energy. This shortens the charging time, which in turn helps to increase the number of attended sensor nodes. Also, the selection of optimal system parameters for each of the four cases discussed in previous section is important to assess the deviation from ideal case along with the severity of mismatches. For this purpose, an optimization problem for k^{th} case is formulated as follows:

$$(\mathbf{P1}): \quad \underset{h,n}{\text{minimize}} \quad P_{tx}^{(k)}$$
$$\text{s. t.: } (\mathbf{C1}): \ P_{rx}^{(k)}(h,n) \geq P_0, \quad (20)$$
$$(\mathbf{C2}): \ h_{min} \leq h \leq h_{max},$$
$$(\mathbf{C3}): \ n_{min} \leq n \leq n_{max},$$

The objective of (**P1**) is to select hovering altitude h and antenna exponent n, such that the transmitted power level can be minimized while guaranteeing a received power threshold P_0. Constraint (**C1**) takes the advantage of saturation region of energy harvester [33], because the harvested power does not increase beyond a certain received power level P_0. In other words, receiving a power level beyond P_0 is not beneficial, because no further increase in harvested power is noted with increase in the level of received power. Constraint (**C2**) restricts the operational altitude of UAV, whereas constraint (**C3**) restricts the antenna exponent range. This problem can be interpreted as follows: the energy consumption in communication related stuff can be controlled, whereas energy consumption of UAV in mechanical operation is not of our interest in the given context.

(**P1**) needs to be solved separately for all the four cases ($k = \{1, 2, 3, 4\}$). Based on the expressions of received power for different cases obtained in (6), (8), (13), and (17), they can be written in generalized form as follows:

$$P_{rx}^{(k)}(h,n) = P_{tx}^{(k)} \cdot G_0 \cdot W_k(h,n), \quad \text{for } k = \{1,2,3,4\} \quad (21)$$

where the expressions of $W_k(h,n)$ are given in (7), (9), (14), and (18) for $k = 1, 2, 3$, and 4, respectively.

Using the expression of $P_{rx}^{(k)}(h,n)$ in (21), constraint (**C1**) is rewritten as follows:

$$P_{tx}^{(k)} \cdot G_0 \cdot W_k(h,n) \geq P_0 \ \Rightarrow \ P_{tx}^{(k)} \geq \frac{P_0}{G_0 \cdot W_k(h,n)}. \quad (22)$$

From (22) it may be noted that, $P_{tx}^{(k)}$ is inversely proportional to $W_k(h,n)$, as P_0 and G_0 are constants. Therefore, minimizing $P_{tx}^{(k)}$ is equivalent to maximizing $W_k(h,n)$.

Using (22), the optimization problem (**P1**) for k^{th} case can be transformed as follows:

$$(\mathbf{P2}): \quad \underset{h,n}{\text{maximize}} \quad W_k(h,n), \quad \text{for } k = \{1,2,3,4\}$$
$$\text{s. t.: } (\mathbf{C2}) \text{ and } (\mathbf{C3}).$$
$$(23)$$

Thus, solving (**P2**) is equivalent to solving ((**P1**)). It may be noted that, the optimization variable h is continuous, whereas n is discrete. In addition, the closed-form expressions for $W_k(h,n)$ are different for even and odd values of n, which discourages to use integer relaxation. Therefore, the nature of $W_k(h,n)$ against h and n investigated in Lemma 1 to Lemma 6 are used to solve (**P2**) in order to evaluate the optimal system parameters.

A. Optimal Hovering Altitude Estimation

The optimal hovering altitude is obtained for a given value of antenna exponent (say $h^*(n)$), and the characterization done in previous section is used to obtain this. $W_1(h,n)$ is a decreasing function of h for a given value of antenna exponent. Therefore, the minimum hovering altitude is optimal for all n. $W_3(h,n)$ also exhibits the same variation (see Lemma 1) and hence the optimal hovering altitude is minimum for this.

On the other hand, both $W_2(h,n)$ and $W_4(h,n)$ exhibit unimodal variation against hovering altitude for a given value of antenna exponent (see Lemma 1 and Lemma 5). Therefore, *golden section method* is used to find the optimal height $h^*(n)$ for a given n. *Golden section method* is an elimination method, which reduces the computational complexity by eliminating the search intervals in successive iterations [34]. For brevity, the procedures of *golden section method* is not presented here; this is explained in detail in [34]. Here, the accuracy of *golden section method* is considered to be 0.01 m $= 1$ cm during simulation.

In the same way, optimal antenna exponent (say, $n^*(h)$) can be obtained for a given hovering altitude. Towards this, the maximum value of antenna exponent is optimal for a given value of hovering altitude for $W_1(h,n)$ and $W_3(h,n)$. On the other hand, in case of $W_2(h,n)$ and $W_4(h,n)$, the optimal antenna exponents are obtained using *golden section method* due to unimodal nature proved respectively in Lemma 2 and Lemma 6.
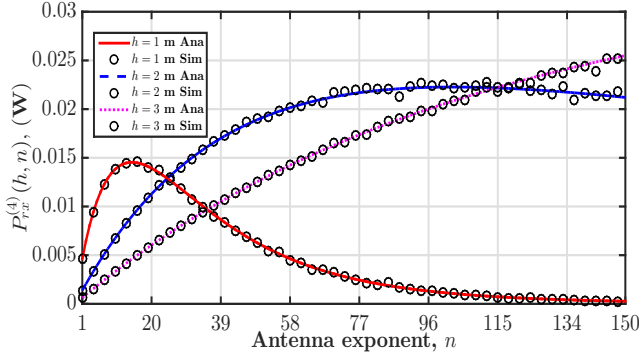
Figure 3: Variation of received power against antenna parameter for different hovering altitude when the sensor node experiences both *LM* as well as *OM*.

B. Optimal System Parameter Estimation

Extending the findings of last subsection, the optimal system parameters, i.e., transmit power, hovering altitude, and antenna exponent, are obtained here. This is obtained by solving (**P2**). For $W_1(h, n)$ and $W_3(h, n)$, the optimal hovering altitude is lowest allowed value h_{min}, whereas optimal antenna exponent is the highest allowed value n_{max}. This can be directly referred from the variation characteristics of $W_1(h, n)$ and $W_3(h, n)$.

On the other hand, for the two other cases, i.e, $W_2(h, n)$ and $W_4(h, n)$, the optimal system parameters need to be evaluated using their variation characteristics. To this end, an algorithm, called *Hovering Inaccuracy-aware Optimal Charging System Design (HI-OCSD)*, is proposed to find the optimal system parameters using the findings in Lemmas 1, 2, 5, and 6. First, the optimal hovering altitude $h_{opt}(n)$ is obtained for a given n followed by the computation of optimal value of $W_k(h_{opt}(n), n)$. Then, the value of $W_k(h^*(n), n)$ is compared with the optimal hovering altitude for the previous value of antenna exponent, i.e., $W_k(h^*(n-1), n-1)$. If increase in $W_k(\cdot)$ is observed compared to the previous one, then the iteration continues and n is increased by one. In contrast, if decrease in $W_k(\cdots)$ is observed compared to previous one then iteration terminates. This is due to the unimodal variation of $W_k(h, n)$ against h and n individually. Thus, the optimal deployment altitude and antenna exponent are obtained. Then, optimal transmitted power is evaluated using these parameters.

The solution obtained by HI-OCSD is global optimal due to unimodal variation of $W_k(h, n)$ against hovering altitude h and antenna exponent n individually. This ensures unique optimal solution over the search space of h for a given n and vice-versa. Therefore, as a sequential optimization h is optimized first, then n is optimized which leads to the global optimal solution.

V. RESULTS AND DISCUSSIONS

Here, the analysis done in the previous sections is numerically evaluated, where the hovering inaccuracy parameters listed in Table I are used for simulation. The numerical values of different parameters considered here are as follows: $P_{tx} = 1$ W, $G_{rx} = 2.10$, $P_o = 45$ mW, $n_{min} = 1$, $n_{max} = 50$, $h_{min} = 1$ m, $h_{max} = 3$ m , $\lambda =$

Algorithm 1 Hovering Inaccuracy-aware Optimal Charging System Design (HI-OCSD)

1: Input: G_0, n_{min}, n_{max}, h_{min}, h_{max}, P_0, Parameters of hovering inaccuracy from Table I
2: Output: P_{tx}^{opt}, h_{opt}, n_{opt}
3: **if** $k = 1$ or $k = 3$ **then**
4:     $h_{opt} = h_{min}$, $n_{opt} = n_{max}$
5:     Calculate $W_k(h_{opt}, n_{opt})$
6:     $P_{tx}^{opt} = \frac{P_0}{G_0 \cdot W_k(h_{opt}, n_{opt})}$
7: **end if**
8: **end**
9: **if** $k = 2$ or $k = 4$ **then**
10:     $\Delta = 1$, $n = n_{min}$
11:     Calculate $h^*(n)$ for given n using *golden-section method*
12:     Calculate $W_k(h^*(n), n)$
13:     **while** $\Delta \geq 0$ **do**
14:         $n = n + 1$
15:         Calculate $h^*(n)$ for given n using *golden-section method*
16:         Calculate $W_k(h^*(n), n)$
17:         $\Delta = W_k(h^*(n), n) - W_k(h^*(n-1), n-1)$
18:     **end while**
19:     **end**
20:     $n_{opt} = n - 1$, $h_{opt} = h^*(n-1)$
21:     $P_{tx}^{opt} = \frac{P_0}{G_0 \cdot W_k(h_{opt}, n_{opt})}$
22: **end if**
23: **end**

0.32786 cm (at operating frequency 0.915 GHz). Lower operational altitude is preferred for UAV-aided RFET due to poorer sensitivity in RFET application, which restricts the operational range of energy transfer up to a few meters. Also, a higher power transfer is ensured at lower UAV hovering altitude.

A. Impact of Hovering Inaccuracy

The variation of received power against antenna exponent n for different deployment altitude h, where the sensor node experiences both *LM* as well as *OM*, is shown in Fig. 3. The values obtained from simulation matches closely with that obtained from analysis. This validates accuracy of the closed-form expression in (17). To quantify the closeness and matching between simulated and analytically computed values, root mean square error (RMSE) between them is evaluated. The RMSE values obtained from analysis with respect to simulation results are 1.41×10^{-4}, 3.67×10^{-4}, and 1.72×10^{-4} for hovering altitude of 1 m, 2 m, and 3 m, respectively. The values of RMSE also indicate that simulated and analytically computed values match closely. The value of RMSE is highest for $h = 2$ m and it is least for $h = 1$ m, because the value of received power is relatively higher for $h = 2$ m, whereas it is relatively lesser for $h = 1$ m.

It may be noted that, the received power first increases then decreases. This is because, the half-power beam width of antenna radiation pattern (see (4)) reduces with increase in the value of antenna exponent n. The antenna with a narrower
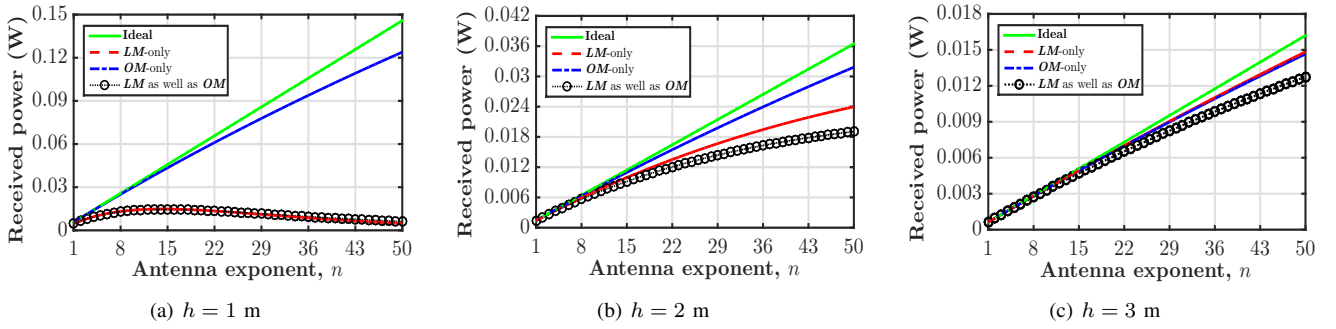
Figure 4: Variation of received power for different cases against antenna exponent for different hovering altitude.

beam width has lesser projection area on the ground. Also, a smaller value of n offers a larger ground projection area with lesser gain. As the value of n increases, the projection area reduces and the gain increases, which leads to increase in the received power. The gain of antenna overcomes this narrowness of beam up to some higher value of n. But, if n continues to increase, the target sensor node tends to lie outside the ground projection area of the beam; the effect of reduced beam width becomes severe and unacceptable at further higher values of n.

On the other hand, for a given value of antenna exponent n, projection area of the antenna's beam on the ground increases with increase in hovering altitude h, and thus the increased beam projection area easily covers the ground sensor location. Although the path loss increases with increase in value of h, a higher gain of antenna dominates the path loss, thereby aiding in RFET. Therefore, the received power is higher for a higher value of h, as observed in Fig. 3. However, if h continues to increase, the path loss eventually dominates the effect of large value of n. This leads to an increase and then decrease in received power with hovering altitude h.

The variation of received power against antenna exponent for all the four cases characterized in Section III are shown in Fig. 4 for different hovering altitude. It can be observed that, the hovering inaccuracy has notable impact on the performance, as received power deviates significantly in presence of hovering inaccuracy compared to ideal one. The deviation caused by *LM* is more severe than that of *OM*, as received power due to *OM* is very close to ideal one. In case of *LM*, the distance as well as elevation angle both changes, whereas only elevation angle changes in case of *OM*. It may be noted that, the performance deviation is higher at lower hovering altitude and approaches to ideal one with increase in hovering altitude. *LM* and *OM* both are effective at lower altitude, and their impact decreases with increase in altitude. The positioning error does not increase in the proportionate way with increase in the height, therefore the impact of *LM* reduces with height. In contrast, the elevation angle (mean and variance) decreases with increase in height. At lower hovering altitude, the pushed down air while hovering reverts back and collides with UAV at low altitude operation. Due to this, UAV vibrates it little bit more compared to that at a higher altitude, as the pushed down air has more space to dissipate at higher hovering altitude. Hence, stability increases due to less turbulence at a higher

altitude.

Remark 6. *RFET performance degrades severely in presence of hovering inaccuracy, which cannot be ignored in UAV-aided RFET system design. The impact of LM on the performance is more severe than that of OM.*

B. Optimal Selection of System Parameters

The variation of optimal hovering altitude $h^*(n)$ against antenna exponent n is shown in Fig. 5(a). For ideal as well as *OM*-only scenarios, the lowest possible altitude h_{min} is the optimal for all values of n, which approves the finding in Lemma 3. For other two cases, i.e., with *LM*-only and with *LM* as well as *OM*, $h^*(n)$ is the lowest for a smaller value of n, whereas it increases with increase in the value of antenna exponent n. For a smaller value of n, the beam width is high, which covers the sensor node sufficiently due to large projection area of beam on the ground. Therefore, lowest height is optimal as the distance between transmitter and receiver is the least.

In contrast, the beam of transmitter antenna becomes narrower as n increases, and UAV increases its hovering altitude to overcome this. The increase in hovering altitude has two benefits. First, larger projection area on the ground easily covers the sensor node. Second, the impact of hovering inaccuracy decreases with increase in hovering altitude. However, if the hovering altitude continues to increase beyond $h^*(n)$, then the path loss factor dominates the antenna gain. Likewise, if UAV hovers below $h^*(n)$, then the antenna is not able to cover the sensor node.

From Fig. 5(a) it may be noted that the optimal height in case of LM-only is relatively higher than in case of LM as well as OM for smaller values of antenna exponent n. On the other hand, the optimal height in case of LM as well as OM is relatively higher than the case with LM-only for a higher value of n. The elevation angle θ is a random variable in case of LM as well as OM, whereas it is constant in case of LM-only. For a smaller value of n, larger ground projection area of antenna beam ensures easier coverage of sensor node at a lower altitude. In addition, the randomness in elevation angle helps to cover the sensor node with lesser elevation angle due to larger projection area, which aids in the performance at relatively lower altitude in case of LM as well as OM. On the other hand, for higher values of n, the randomness in
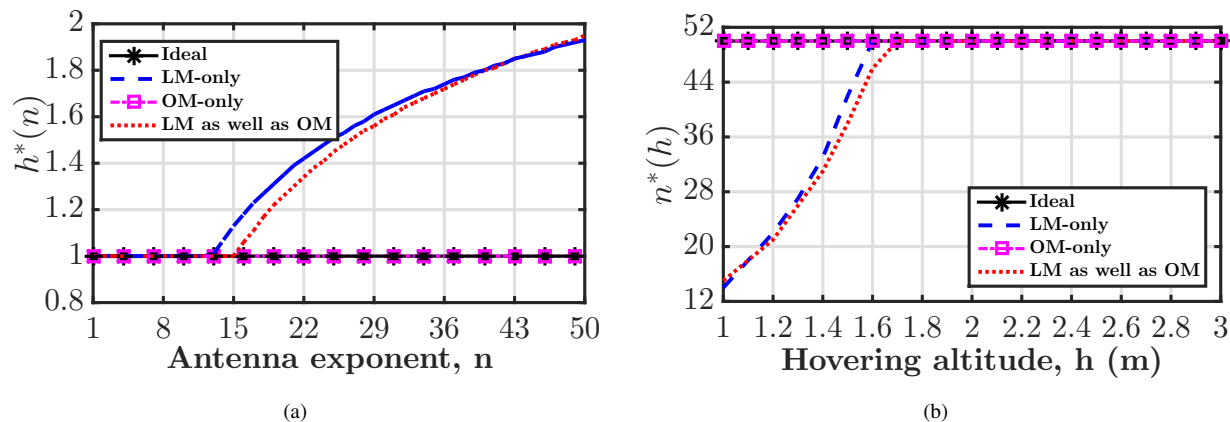
(a)

(b)

Figure 5: Variation of (a) optimal hovering altitude against antenna exponent, and (b) optimal antenna exponent against hovering altitude for different cases.
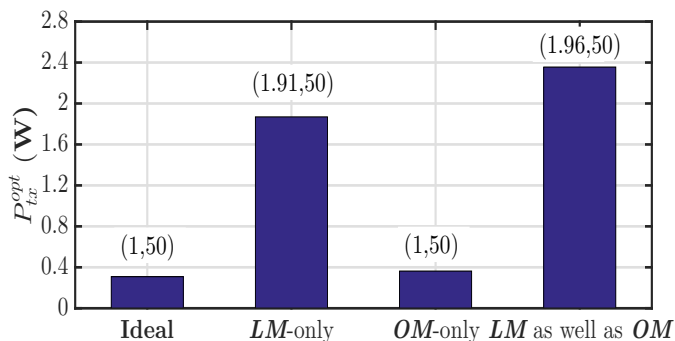

Figure 6: Variation of optimal system parameters for different cases.

elevation angle and the smaller ground projection area do not easily ensure the coverage of sensor node at a relatively lower altitude in case of LM as well as OM as compared to LM-only. Therefore, UAV hovers at a slightly higher altitude to enlarge the ground coverage area and to reduce the effect of randomness in order to meet the performance criteria.

The variation of optimal value of antenna exponent is shown in Fig. 5(b) for different hovering altitude. For ideal and *OM*-only scenarios, the highest value of antenna exponent is optimal for all hovering altitude, which approves the finding in Lemma 4. For the other two cases, i.e., with *LM*-only and *LM* as well as *OM*, $n^*(h)$ increases initially and saturates up to a maximum value of antenna exponent n_{max}. At lower altitude, the effect of hovering inaccuracy is higher, and hence a wider beam width is required to cover the sensor node for RFET. On the other hand, a narrow beam offers sufficient coverage area at a higher hovering altitude. Thus, maximum allowed value of antenna exponent n_{max} is optimal.

The optimal system parameters (transmit power level, hovering altitude, and antenna exponent) estimated using *HI-OCSD* algorithm are shown in Fig. 6 for different cases discussed in Section III. One can observe that, the optimal transmit power level is least for ideal scenario, whereas the same is highest when the sensor node experiences both of the mismatches, i.e., *LM* as well as *OM*. It may also be noted that, *LM* dominated *OM*, and *LM* affects the performance more severely. The optimal antenna exponent is the maximum value, i.e.,

n_{max}, for all the four cases. On the other hand, optimal hovering altitude is minimum h_{min} for ideal and *OM*-only cases. UAV increases its altitude to overcome the effect of hovering inaccuracy in two other cases. Fig. 6 indicates that, if the sensor nodes is charged assuming ideal hovering scenario, i.e., then may not be able to operate up to the desired time, as it receives and harvests lesser power. Therefore, its inclusion in the analysis is essential for accurate design as well as to ensure uninterrupted operation of sensor nodes.

Remark 7. *If hovering inaccuracy of UAV is not taken into consideration in UAV-aided sustainable IoT networking framework, then the possibility of under-provisioning of resources in UAV-aided RFET is very high.*

VI. CONSIDERATION OF DIFFERENT LEVEL OF HOVERING INACCURACY

The hovering inaccuracy parameters listed in Table I have been used in performance evaluation (Section V). The parameter values in Table I have been obtained based on the model developed from extensive field measurements in an open area (hockey ground of IIT Delhi), where a total of nine GPS satellites were available without multipath signals. This can be thought of as ideal deployment scenario. In contrary, the purpose of deploying UAV-aided RFET is to ensure the charging of sensor nodes located in hard-to-reach or arduous locations. In these scenarios, UAV is expected to undergo different level of hovering inaccuracy will be very different from open area and UAV will undergo different level of hovering inaccuracy other than that mentioned in Table I while facilitating RFET. In this section, different level of hovering inaccuracy are modeled and system parameters are optimized.

A. Modeling of Different Level of Hovering Inaccuracy

As noted in previous section, impact of *LM* on performance is more severe; even *LM* dominates *OM*. Using this observation, different level of *LM* is considered in order to realize different level of hovering inaccuracy as *LM* is the dominant component of hovering inaccuracy. On the other hand, *OM* is considered to be the same as listed in Table I, because

UAV experiences almost similar angular displacement. This argument is reasonable while modeling different level of hovering inaccuracy, because the deviation in performance due to only *OM* is not remarkable.

The deviation in horizontal distance, i.e., the difference between the location of ground sensor node and the ground projection point of the hovering UAV, obtained from experimental measurements (see Table I), is expressed as:

$$l_o(h) = \sqrt{d^2(h) - h^2} = \sqrt{(u_1 - 1)h^2 + u_2 h + u_3}. \quad (24)$$

Using (24) and a tuning parameter $\alpha > 0$, different level of *LM* is considered. The distance between ground node and the ground projection point of UAV is denoted as:

$$l^{(\alpha)}(h) = \alpha \cdot l_o(h). \quad (25)$$

The tuning parameter α is physically interpreted as follows: $0 < \alpha < 1$ indicates that the level of *LM* is lesser than that obtained in Table I. Here, the number of satellites available in the deployment scenario is high with negligible effect of multipath propagation of satellite signals from surrounding, which offers better accuracy. $\alpha = 1$ indicates that the *LM* is same as in Table I. Likewise, $\alpha > 1$ indicates that *LM* is higher than that obtained in Table I. Here, the number of satellites available in the deployment scenario is less with significant effect of multipath propagation of satellite signals from surrounding, which offers relatively less accuracy.

With this formulation, the distance between UAV-mounted transmitter and ground sensor node is expressed as:

$$d^{(\alpha)}(h) = \sqrt{h^2 + (l^{(\alpha)}(h))^2} = \sqrt{h^2 + \alpha^2 \cdot (l_o(h))^2}. \quad (26)$$

Similarly, the elevation angle between UAV-mounted transmitter and ground sensor node due to *LM* is expressed as:

$$\Phi_{LM}^{(\alpha)}(h) = \arctan\left[\frac{l^{(\alpha)}(h)}{h}\right]. \quad (27)$$

Till now, distance and elevation angle due to *LM* were obtained for different level of hovering inaccuracy (see (26)). However, the actual elevation angle considering both *LM* and *OM* with different level of hovering inaccuracy is not known. For this purpose, the bounds on elevation angle in (1) that account for both *LM* and *OM* are used. Referring to the bounds, the following can be written in the given context:

$$\Phi_{LM}^{(\alpha)}(h) - \Phi_{OM}(h) \leq \Theta^{(\alpha)}(h) \leq \Phi_{LM}^{(\alpha)}(h) + \Phi_{OM}(h)$$
$$\Rightarrow \quad \Theta_{min}^{(\alpha)}(h) \leq \Theta^{(\alpha)}(h) \leq \Theta_{max}^{(\alpha)}(h) \quad (28)$$

where $\Theta_{min}^{(\alpha)}(h) = \Phi_{LM}^{(\alpha)}(h) - \Phi_{OM}(h)$ and $\Theta_{max}^{(\alpha)}(h) = \Phi_{LM}^{(\alpha)}(h) + \Phi_{OM}(h)$.

$\Theta_{min}^{(\alpha)}$ is also a Gaussian random variable, which is a linear transformed version of $\Phi_{OM}(h)$. Its mean ($\mu_{min}^{(\alpha)}(h)$) and standard deviation ($\sigma_{min}^{(\alpha)}(h)$) are given by:

$$\mu_{min}^{(\alpha)}(h) = \Phi_{LM}^{(\alpha)}(h) - \mu_{OM}(h), \quad \sigma_{min}^{(\alpha)}(h) = \sigma_{OM}(h). \quad (29)$$

Θ_{max}^{dev} is also a Gaussian random variable, which is a linear transformed version of $\Phi_{OM}(h)$. Its mean ($\mu_{max}^{dev}(h)$) and standard deviation ($\sigma_{max}^{dev}(h)$) are given by:

$$\mu_{max}^{(\alpha)}(h) = \Phi_{LM}^{(\alpha)}(h) + \mu_{OM}(h), \quad \sigma_{max}^{(\alpha)}(h) = \sigma_{OM}(h). \quad (30)$$

B. Selection of Optimal System Parameters

As discussed above, different level of hovering inaccuracy is modeled using a tuning parameter α, which leads to change in distance as well as elevation angle between transmitter and receiver by including the effect of both mismatches. Using the bound of $\Theta^{(\alpha)}(h)$ in (28), UAV-aided RFET performance is evaluated for the following cases:

- *Case 1*: No hovering inaccuracy (Ideal)
- *Case 2:* Distance: $d^{(\alpha)}(h)$,
  Elevation angle: $\Theta_{min}^{dev} \sim \mathcal{N}\left(\mu_{min}^{(\alpha)}(h), \sigma_{min}^{(\alpha)}(h)\right)$
- *Case 3:* Distance: $d^{(\alpha)}(h)$,
  Elevation angle: $\Phi_{LM}^{dev}(h)$
- *Case 4:* Distance: $d^{(\alpha)}(h)$,
  Elevation angle: $\Theta_{min}^{dev} \sim \mathcal{N}\left(\mu_{max}^{(\alpha)}(h), \sigma_{max}(h)\right)$.

The characteristics in terms of received power for these three cases are investigated, and their natures are found to be unimodal as stated in Lemma 5 and Lemma 6. Thus, the proposed algorithm *HI-OCSD* remains valid for these three cases in order to obtain the optimal system parameters. For brevity, the proofs are not mentioned here. In the proposed framework, the value of α itself indicates a practical deployment scenario having α-dependent hovering profile. Therefore, α cannot be optimized, as it represents a deployment scenario. However, for a given deployment scenario, it is required to optimize the operating system parameters, as conducted in this study.

It can be observed from Fig. 7(a) that, in all the three cases, the optimal transmitted power increases as α increases, because the distance between UAV-mounted transmitter and ground receiver increases with α. The optimal transmit power for ideal case is less compared to other three cases, and the deviation in this parameter increases with increase of hovering inaccuracy. On the other hand, the optimal transmit power for $\Phi_{LM}^{(\alpha)}$ lies in between $\Theta_{min}^{(\alpha)}$ and $\Theta_{max}^{(\alpha)}$, whereas it is maximum for $\Theta_{max}^{(\alpha)}$. Although the distance between transmitter and receiver is same for all these three cases for a given value of α, but the randomness in elevation angle is highest for $\Theta_{max}^{(\alpha)}$ (see (30)). This requires a higher beam width of antenna, which has lower gain. Thus, relatively higher power needs to be transmitted to overcome the randomness.

The variation of optimal hovering altitude is shown in Fig. 7(b) against α. In ideal case, the optimal altitude is the lowest possible value. In other three cases, the lowest possible altitude is optimal for smaller values of tuning parameter, because the distance between transmitter and receiver is less and the antenna's beam has sufficient projection area on ground to cover the sensor node. With increased tuning parameter value, UAV shifts its altitude up. This is because, the elevation angle between UAV-mounted transmitter and ground receiver increases with increase in α (see (25)). Hence, a higher altitude of UAV offers larger projection area of antenna's beam on ground, which comfortably covers the sensor node.
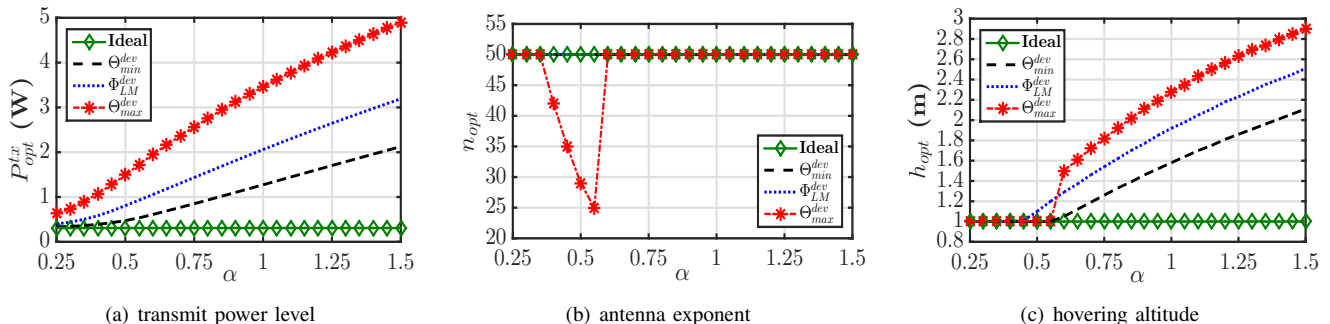
Figure 7: Variation of optimal system parameters for different level of hovering inaccuracy.

The variation of optimal antenna exponent is shown in Fig. 7(c), which is the maximum allowed value n_{max} in ideal case, $\Theta_{min}^{(\alpha)}$ and $\Phi_{LM}^{(\alpha)}$. In contrast, this value first decreases and then saturates up to maximum allowed value for $\Theta_{max}^{(\alpha)}$, because the randomness in elevation angle is very high for $\Theta_{max}^{(\alpha)}$, and antenna having a higher beam width overcomes this randomness. Also, optimal height is the minimum allowed value in this range of α (see Fig. 7(b)), which offers reduction in antenna exponent or increase in antenna beam width. As α increases, the optimal value of antenna exponent saturates towards the maximum allowed value. In these range of α, the optimal hovering altitude also continues to increase, which leads to increase in antenna exponent. The value of antenna gain in these range dominates the distance based path loss.

Remark 8. *UAV moves up as the level of hovering inaccuracy increases, because the projection area of transmitter antenna beam on the ground increases with increase in hovering altitude and the sensor node lies within it.*

Remark 9. *UAV hovering condition strongly impacts the optimal selection of system parameters, which demands hovering inaccuracy parameters to be included in system design.*

VII. CONCLUDING REMARKS

The performance analysis of UAV-aided RFET system in presence of hovering inaccuracy has been investigated. Hovering inaccuracy comprises of two types of mismatches: *Localization mismatch (LM)* and *Orientation mismatch (OM)*. This leads to change in distance as well as elevation angle between the transmitter (mounted on UAV) and the receiver (sensor node deployed on ground). The effect of these mismatches (individual and joint) on received power has been analyzed, and a closed-form expressions for received power has been obtained for a generalized radiation pattern of antenna. To evaluate the optimal system parameters, the formulated optimization problem has been noted to be a mixed nature of variables. To solve this optimization problem, an algorithm, called *Hovering Inaccuracy-aware Optimal Charging System Design (HI-OCSD)* has been proposed. The simulation results indicate a remarkable deviation of performance from ideal scenario due to hovering inaccuracy as compared to ideal scenario. Thus, inclusion of hovering inaccuracy is essential in UAV-aided RFET system design. A study comprising different level of hovering inaccuracy to account for different deployment area

has also been illustrated, which indicates that UAV needs to hover at higher altitude as hovering inaccuracy increases.

Further investigations on the study of charging mechanism design with different topology of receivers in presence of hovering inaccuracy would be of future research interest, where the impact of different parameters on the performance needs to be investigated. Additionally, multiple UAV coordination during the design of new charging protocols for enhanced performance is another interesting direction.

APPENDIX

A. Proof of Lemma 1

For a function to be unimodal function, the first derivative should change sign at most once. The derivative of $W_2(h, n)$ with respect to h at $n = n_0$ is obtained as,

$$
\begin{aligned}
\frac{d}{dh}W_2(h, n_0) =& 2(n_0+1)\Big[\frac{-1}{d^2(h)} \cdot n_0 \cos^{n_0-1}(\Phi_{LM}(h))\cdot \\
& \sin(\Phi_{LM}(h)) \cdot \Phi'_{LM}(h) + \cos^{n_0}(\Phi_{LM}(h))\cdot \\
& \frac{-(2u_1h + u_2)}{d^4(h)}\Big] \\
=& -2(n_0+1) \cdot \frac{1}{d^4(h)} \cdot \cos^{n_0-1}(\Phi_{LM}(h))\cdot \\
& \Big[n_0 d^2(h)\Phi'_{LM}(h) \cdot \sin(\Phi_{LM}(h)) \\
& + (2u_1h + u_2) \cdot \cos(\Phi_{LM}(h))\Big]
\end{aligned}
$$

where $\Phi'_{LM}(h) = \frac{d}{dh}\Phi_{LM}(h) = 3v_1h^2 + 2v_2h + v_3$. $\Phi'_{LM}(h) < 0 \; \forall h$, because the discriminant of $\Phi'_{LM}(h)$, i.e., $4v_2^2 - 12v_1v_3$ is negative and $v_1 < 0$ (see Table I). $\frac{d}{dh}W_2(h, n_0)$ can be rewritten as follows:

$$
\begin{aligned}
\frac{d}{dh}W_2(h, n_0) =& -2(n_0+1) \cdot \frac{1}{d^4(h)} \cdot \cos^{n_0-1}(\Phi_{LM}(h))\cdot \\
& Z(h) \cdot \cos\Big(\Phi_{LM}(h) - \theta_0\Big)
\end{aligned}
$$

where $Z(h) = \sqrt{(n_0 d^2(h)\Phi'_{LM}(h))^2 + (2u_1h + u_2)^2}$ and

$$
\theta_0 = \arcsin\frac{n_0 d^2(h)\Phi'_{LM}(h)}{Z(h)}.
$$

From the variation of $\frac{d}{dh}W_2(h, n_0)$ against hovering altitude h in Fig. A-1 for different values of antenna exponent n_0 it is observed that the sign of derivative changes once for some values of n_0; it does not change for the other values of n_0.
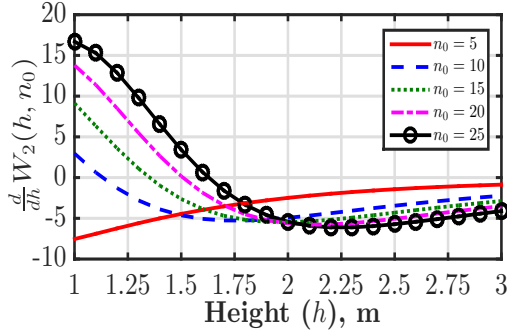
Figure A-1: The variation of $\frac{d}{dh}W_2(h, n_0)$ against height for different values of antenna exponent.
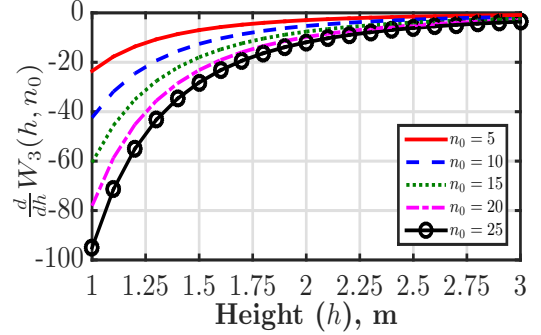

Figure C-1: The variation of $\frac{d}{dh}W_3(h, n_0)$ against height with antenna exponent as the parameter.

B. Proof of Lemma 2

In case of discrete variable, the first derivative is obtained from successive difference. Thus, the first derivative of $W_2(h, n)$ for a given hovering altitude $h = h_0$ is,

$$
\begin{aligned}
(\Delta W_2(h_0, n))_n &= W_2(h_0, n) - W_2(h_0, n - 1) \\
&= \frac{1}{d^2(h_0)} \cdot \Big[2(n + 1) \cdot \cos^n(\Phi_{LM}(h_0)) - \\
&\quad 2(n) \cdot \cos^{n-1}(\Phi_{LM}(h_0)) \Big] \\
&= \frac{1}{d^2(h_0)} \cdot \cos^{n-1}(\Phi_{LM}(h_0)) \cdot \Big[(n + 1) \\
&\quad \cdot \cos(\Phi_{LM}(h_0)) - n \Big].
\end{aligned}
$$

$(\Delta W_2(h_0, n))_n$ is equated to 0 in order to obtain the value of n around which $(\Delta W_2(h_0, n))_n$ changes its sign. $(\Delta W_2(h_0, n))_n = 0$ condition leads to the two cases:
Case 1: $\cos^{n-1}(\Phi_{LM}(h_0)) = 0$. This is not possible because $0 \leq \Phi_{LM}(h) < \pi/2$.
Case 2: $(n + 1) \cdot \cos(\Phi_{LM}(h_0)) - n = 0$. This leads to $n = \frac{\cos(\Phi_{LM}(h_0))}{1 - \cos(\Phi_{LM}(h_0))} = n_{th}$(say). n_{th} is unique as $0 \leq \Phi_{LM}(h) < \pi/2$.
Thus, $(\Delta W_2(h_0, n))_n$ will change its sign about n_{th} if $n_{th} < n_{max}$; otherwise (if $n_{th} \geq n_{max}$) it will not change its sign. Thus, $(\Delta W_2(h_0, n))_n$ changes its sign at most once, which proves its unimodal nature against antenna exponent.

C. Proof of Lemma 3

For a function to be non-increasing, the first derivative should be less than or equal to zero. The derivative of $W_3(h, n)$ with respect to h at $n = n_0$ is obtained as,

$$
\begin{aligned}
\frac{d}{dh}W_3(h, n_0) &= \begin{cases} \frac{-2}{h^3} \cdot X_{even}(h, n_0) + \\ \quad \frac{1}{h^2} \cdot F_1(h, n_0), & \text{if } n_0 = \text{even} \\ \frac{-2}{h^3} \cdot X_{odd}(h, n_0) + \\ \quad \frac{1}{h^2} \cdot G_1(h, n_0), & \text{if } n_0 = \text{odd} \end{cases} \\
&= \begin{cases} W_3(h, n_0) \cdot \frac{-2}{h} + \\ \quad \frac{1}{h^2} \cdot F_1(h, n_0), & \text{if } n_0 = \text{even} \\ W_3(h, n_0) \cdot \frac{-2}{h} + \\ \quad \frac{1}{h^2} \cdot G_1(h, n_0), & \text{if } n_0 = \text{odd} \end{cases}
\end{aligned}
$$

where $X_{even}(h, n_0)$ and $X_{odd}(h, n_0)$ are given in (14). $F_1(h, n_0)$ and $G_1(h, n_0)$ are given in (C.1).

$$
\begin{aligned}
F_1(h, n_0) &= \frac{1}{2^{n_0-1}} \Big[\sum_{r=0}^{\frac{n_0}{2}-1} \binom{n_0}{r} \cos((n_0 - 2r)\mu_{OM}(h)) \cdot \\
&\quad \exp\Big(-\frac{1}{2}\sigma_{OM}^2(h)(n_0 - 2r)^2 \Big) \cdot (-\sigma_{OM}(h)) \cdot (n_0 - 2r)^2 \\
&\quad \sigma_{OM}'(h) + \exp\Big(-\frac{1}{2}\sigma_{OM}^2(n_0 - 2r)^2 \Big) \cdot \\
&\quad (-\sin((n_0 - 2r)\mu_{OM})) \cdot (n_0 - 2r)\mu_{OM}'(h) \Big] \\
G_1(h, n_0) &= \frac{1}{2^{n_0-1}} \Big[\sum_{r=0}^{\frac{n_0-1}{2}} \binom{n_0}{r} \cos((n_0 - 2r)\mu_{OM}(h)) \cdot \\
&\quad \exp\Big(-\frac{1}{2}\sigma_{OM}^2(h)(n_0 - 2r)^2 \Big) \cdot (-\sigma_{OM}(h)) \cdot (n_0 - 2r)^2 \cdot \\
&\quad \sigma_{OM}'(h) + \exp\Big(-\frac{1}{2}\sigma_{OM}^2(n_0 - 2r)^2 \Big) \cdot \\
&\quad (-\sin((n_0 - 2r)\mu_{OM})) \cdot (n_0 - 2r)\mu_{OM}'(h) \Big]
\end{aligned}
\tag{C.1}
$$

where $\mu_{OM}'(h) = \frac{d}{dh}\mu_{OM}(h) = 3w_1h + 3w_2h + w_3$ and $\sigma_{OM}'(h) = \frac{d}{dh}\sigma_{OM}(h) = 3z_1h + 3z_2h + z_3$.

The variation of $\frac{d}{dh}W_3(h, n_0)$ in Fig. C-1 for different values of n_0 shows, the sign of $\frac{d}{dh}W_3(h, n_0)$ is non-positive, which proves its non-increasing nature against h.

D. Proof of Lemma 4

First derivative of $W_3(h, n)$ with respect to n for a given altitude $h = h_0$ is obtained as,

$$
(\Delta W_3(h_0, n))_n = \frac{1}{h^2} \cdot \begin{cases} X_{even}(h_0, n) - \\ \quad X_{odd}(h_0, n), & \text{if } n = \text{even} \\ X_{odd}(h_0, n) - \\ \quad X_{even}(h_0, n), & \text{if } n = \text{odd} \end{cases}
$$

where $X_{even}(h_0, n)$ and $X_{odd}(h_0, n)$ are given in (14).

The variation of $(\Delta W_3(h_0, n))_n$ against n in Fig. D-1 for different altitude demonstrates non-positivity of $(\Delta W_3(h_0, n))_n$, which proves its non-decreasing nature.
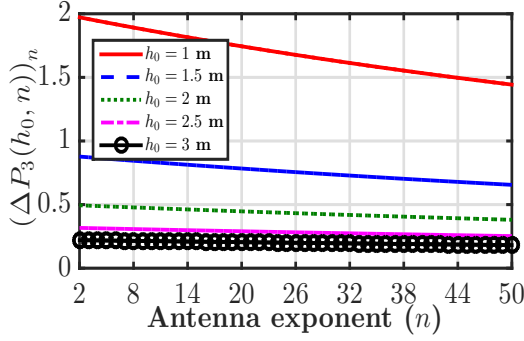
Figure D-1: The variation of $(\Delta P_3(h_0, n))_n$ against antenna exponent with altitude as the parameter.

Figure E-1: The variation of $\frac{d}{dh} W_4(h, n_0)$ against height with antenna exponent as the parameter.

E. Proof of Lemma 5

First derivative of $W_4(h, n)$ with respect to h at $n = n_0$ is obtained as,

$$
\frac{d}{dh} W_4(h, n_0) = \begin{cases} \frac{-(2u_1 h + u_2)}{d^2(h)} \cdot Y_{even}(h, n_0) + \\ \quad \frac{1}{d^2(h)} \cdot F_2(h, n_0), & \text{if } n_0 = \text{even} \\ \frac{-(2u_1 h + u_2)}{d^2(h)} \cdot Y_{odd}(h, n_0) + \\ \quad \frac{1}{h^2} \cdot G_2(h, n_0), & \text{if } n_0 = \text{odd} \end{cases}
$$

$$
= \begin{cases} W_4(h, n_0) \cdot \frac{-(2u_1 h + u_2)}{d^2(h)} + \\ \quad \frac{1}{d^2(h)} F_2(h, n_0) & \text{if } n_0 = \text{even} \\ W_4(h, n_0) \cdot \frac{-(2u_1 h + u_2)}{d^2(h)} + \\ \quad \frac{1}{d^2(h)} G_2(h, n_0) & \text{if } n_0 = \text{odd} \end{cases}
$$

where $Y_{even}(\cdot)$ and $Y_{odd}(\cdot)$ are given in (18). $F_2(\cdot)$ and $G_2(\cdot)$ are given in (E.1).

$$
\begin{aligned}
F_2(h, n_0) = \frac{1}{2^{n_0 - 1}} \Big[& \sum_{r=0}^{\frac{n_0}{2} - 1} \binom{n_0}{r} \cos((n_0 - 2r)\mu_M(h)) \cdot \\
& \exp\left(-\frac{1}{2}\sigma_M^2(h)(n_0 - 2r)^2\right) \cdot (-\sigma_M(h)) \cdot \\
& (n_0 - 2r)^2 \sigma_M'(h) + \exp\left(-\frac{1}{2}\sigma_M^2(n_0 - 2r)^2\right) \cdot \\
& (-\sin((n_0 - 2r)\mu_M(h))) \cdot (n_0 - 2r)\mu_M'(h) \Big]
\end{aligned}
$$

$$
\begin{aligned}
G_2(h, n_0) = \frac{1}{2^{n_0 - 1}} \Big[& \sum_{r=0}^{\frac{n_0 - 1}{2}} \binom{n_0}{r} \cos((n_0 - 2r)\mu_M(h)) \cdot \\
& \exp\left(-\frac{1}{2}\sigma_M^2(h)(n_0 - 2r)^2\right) \cdot (-\sigma_M(h)) \cdot \\
& (n_0 - 2r)^2 \sigma_M'(h) + \exp\left(-\frac{1}{2}\sigma_M^2(n_0 - 2r)^2\right) \cdot \\
& (-\sin((n_0 - 2r)\mu_M(h))) \cdot (n_0 - 2r)\mu_M'(h) \Big]
\end{aligned}
$$

(E.1)

where $\mu_M'(h) = \frac{d}{dh}\mu_M(h) = 3a_1 h + 3a_2 h + a_3$ and $\sigma_M'(h)\frac{d}{dh}\sigma_M(h) = 3b_1 h + 3b_2 h + b_3$.

The variation of $\frac{d}{dh} W_4(h, n_0)$ in Fig. E-1 for different values of n_0 indicates that, the sign of $\frac{d}{dh} W_3(h, n_0)$ changes its sign for some values of n_0, whereas it does not change for the other values. Thus, $\frac{d}{dh} W_4(h, n_0)$ changes its sign at most once, which proves its unimodal nature with respect to h.
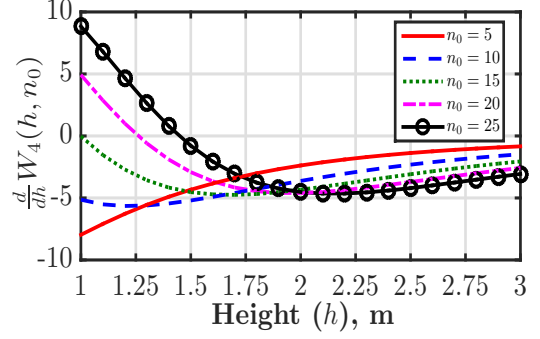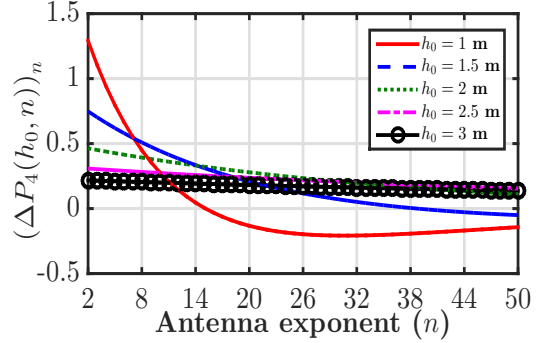

Figure F-1: The variation of $(\Delta P_4(h_0, n))_n$ against antenna exponent with altitude as the parameter.

F. Proof of Lemma 6

First derivative of $W_4(h, n)$ with respect to n at a given altitude $h = h_0$ is found as,

$$
(\Delta W_4(h_0, n))_n = \frac{1}{h^2} \begin{cases} Y_{even}(h_0, n) - \\ \quad Y_{odd}(h_0, n), & \text{if } n = \text{even} \\ Y_{odd}(h_0, n) - \\ \quad Y_{even}(h_0, n), & \text{if } n = \text{odd} \end{cases}
$$

where $Y_{even}(h_0, n)$ and $Y_{odd}(h_0, n)$ are given in (18).

The variation of $(\Delta W_4(h_0, n))_n$ against n in Fig. F-1 for different hovering altitudes suggests that, its sign changes only once for some values of h_0; it does not change for the other values of h_0. Thus, $(\Delta W_4(h_0, n))_n$ changes its sign at most once, which proves its unimodality against antenna exponent.

REFERENCES

[1] A. Al-Fuqaha, M. Guizani, M. Mohammadi, M. Aledhari, and M. Ayyash, "Internet of Things: A survey on enabling technologies, protocols, and applications," *IEEE Commun. Surveys Tuts.*, vol. 17, no. 4, pp. 2347–2376, 4th Quart. 2015.

[2] M. Marjani, F. Nasaruddin, A. Gani, A. Karim, I. A. T. Hashem, A. Siddiqa, and I. Yaqoob, "Big IoT data analytics: Architecture, opportunities, and open research challenges," *IEEE Access*, vol. 5, pp. 5247–5261, Mar. 2017.

[3] B. Martinez, M. Montón, I. Vilajosana, and J. D. Prades, "The power of models: Modeling power consumption for IoT devices," *IEEE Sensors J.*, vol. 15, no. 10, pp. 5777–5789, Oct. 2015.

[4] K. Kaushik, D. Mishra, and S. De, "Stochastic solar harvesting characterisation for sustainable sensor node operation," *IET Wireless Sensor Systems*, vol. 9, no. 4, pp. 208–217, Mar. 2019.

[5] J. Kim and C. Kim, "A DC–DC boost converter with variation-tolerant MPPT technique and efficient ZCS circuit for thermoelectric energy harvesting applications," *IEEE Trans. Power Electron.*, vol. 28, no. 8, pp. 3827–3833, Aug. 2013.

[6] J. Kim, J. Kim, M. Sim, S. Kim, and C. Kim, "A single-input four-output (SIFO) AC–DC rectifying system for vibration energy harvesting," *IEEE Trans. Power Electron.*, vol. 29, no. 6, pp. 2629–2633, June 2014.

[7] C. Song, Y. Huang, J. Zhou, J. Zhang, S. Yuan, and P. Carter, "A high-efficiency broadband rectenna for ambient wireless energy harvesting," *IEEE Trans. Antennas Propag*, vol. 63, no. 8, pp. 3486–3495, Aug. 2015.

[8] D. Mishra, S. De, S. Jana, S. Basagni, K. Chowdhury, and W. Heinzelman, "Smart RF energy harvesting communications: Challenges and opportunities," *IEEE Commun. Mag.*, vol. 53, no. 4, pp. 70–78, 2015.

[9] B. Clerckx, A. Costanzo, A. Georgiadis, and N. Borges Carvalho, "Toward 1G mobile power networks: RF, signal, and system designs to make smart objects autonomous," *IEEE Microw. Mag.*, vol. 19, no. 6, pp. 69–82, Sep. 2018.

[10] B. Clerckx, R. Zhang, R. Schober, D. W. K. Ng, D. I. Kim, and H. V. Poor, "Fundamentals of wireless information and power transfer: From RF energy harvester models to signal and system designs," *IEEE J. Sel. Areas Commun.*, vol. 37, no. 1, pp. 4–33, Jan. 2019.

[11] Powercast. [Online]. Available: http://www.powercastco.com

[12] H. Dai, Y. Liu, G. Chen, X. Wu, T. He, A. X. Liu, and H. Ma, "Safe charging for wireless power transfer," *IEEE/ACM Trans. Netw.*, vol. 25, no. 6, pp. 3531–3544, Dec. 2017.

[13] S. De and R. Singhal, "Toward uninterrupted operation of wireless sensor networks," *IEEE Comput.*, vol. 45, no. 9, pp. 24–30, Sep. 2012.

[14] U. Baroudi, "Robot-assisted maintenance of wireless sensor networks using wireless energy transfer," *IEEE Sensors J.*, vol. 17, no. 14, pp. 4661–4671, July 2017.

[15] F. Sangare, Y. Xiao, D. Niyato, and Z. Han, "Mobile charging in wireless-powered sensor networks: Optimal scheduling and experimental implementation," *IEEE Trans. Veh. Technol.*, vol. 66, no. 8, pp. 7400–7410, Aug. 2017.

[16] S. Suman, S. Kumar, and S. De, "UAV-assisted RFET: A novel framework for sustainable WSN," *IEEE Trans. Green Commun. Netw.*, vol. 3, no. 4, pp. 1117–1131, Dec. 2019.

[17] J. Xu, Y. Zeng, and R. Zhang, "UAV-enabled wireless power transfer: Trajectory design and energy region characterization," in *IEEE Int. Conf. Global Commun. (GLOBECOMM Wksp.)*, Dec. 2017, pp. 1–7.

[18] ——, "UAV-enabled wireless power transfer: Trajectory design and energy optimization," *IEEE Trans. Wireless Commun.*, vol. 17, no. 8, pp. 5092–5106, Aug. 2018.

[19] Y. Hu, X. Yuan, J. Xu, and A. Schmeink, "Optimal 1D trajectory design for UAV-enabled multiuser wireless power transfer," *IEEE Trans. Commun.*, vol. 67, no. 8, pp. 5674–5688, Aug. 2019.

[20] H. Wang, J. Wang, G. Ding, L. Wang, T. A. Tsiftsis, and P. K. Sharma, "Resource allocation for energy harvesting-powered D2D communication underlaying UAV-assisted networks," *IEEE Trans. Green Commun. Netw.*, vol. 2, no. 1, pp. 14–24, Mar. 2018.

[21] J. Chen, S. Li, S. Chen, S. He, and Z. Shi, "Q-charge: A quadcopter-based wireless charging platform for large-scale sensing applications," *IEEE Netw.*, vol. 31, no. 6, pp. 56–61, Nov. 2017.

[22] K. Li, W. Ni, E. Tovar, and A. Jamalipour, "On-board deep Q-network for UAV-assisted online power transfer and data collection," *IEEE Trans. Veh. Technol.*, pp. 1–1, 2019.

[23] F. Huang, J. Chen, H. Wang, G. Ding, Z. Xue, Y. Yang, and F. Song, "UAV-assisted SWIPT in Internet of Things with power splitting: Trajectory design and power allocation," *IEEE Access*, vol. 7, pp. 68 260–68 270, June 2019.

[24] S. Yin, Y. Zhao, and L. Li, "UAV-assisted cooperative communications with time-sharing SWIPT," in *IEEE Int. Conf. Commun. (ICC)*, 2018.

[25] F. Zhou, Y. Wu, R. Q. Hu, and Y. Qian, "Computation rate maximization in UAV-enabled wireless-powered mobile-edge computing systems," *IEEE J. Sel. Areas Commun.*, vol. 36, no. 9, pp. 1927–1941, Sep. 2018.

[26] Y. Du, K. Yang, K. Wang, G. Zhang, Y. Zhao, and D. Chen, "Joint resources and workflow scheduling in UAV-enabled wirelessly-powered MEC for IoT systems," *IEEE Trans. Veh. Technol.*, vol. 68, no. 10, pp. 10 187–10 200, Oct. 2019.

[27] S. Hayat, E. Yanmaz, and R. Muzaffar, "Survey on unmanned aerial vehicle networks for civil applications: A communications viewpoint," *IEEE Commun. Surveys Tuts.*, vol. 18, no. 4, pp. 2624–2661, 4th Quart. 2016.

[28] S. Suman, S. Kumar, and S. De, "Impact of hovering inaccuracy on UAV-aided RFET," *IEEE Commun. Lett.*, vol. 23, no. 12, pp. 2362–2366, Dec. 2019.

[29] M. Mozaffari, W. Saad, M. Bennis, and M. Debbah, "Mobile unmanned aerial vehicles (UAVs) for energy-efficient Internet of Things communications," *IEEE Trans. Wireless Commun.*, vol. 16, no. 11, pp. 7574–7589, Nov. 2017.

[30] S. Suman, S. Kumar, and S. De, "Path loss model for UAV-assisted RFET," *IEEE Commun. Lett.*, vol. 22, no. 10, pp. 2048–2051, Oct. 2018.

[31] Y. Zeng, X. Xu, and R. Zhang, "Trajectory design for completion time minimization in UAV-enabled multicasting," *IEEE Trans. Wireless Commun.*, vol. 17, no. 4, pp. 2233–2246, Apr. 2018.

[32] C. A. Balanis, *Antenna Theory: Analysis and Design*. John Wiley & Sons, 2005.

[33] E. Boshkovska, D. W. K. Ng, N. Zlatanov, and R. Schober, "Practical non-linear energy harvesting model and resource allocation for SWIPT systems," *IEEE Commun. Lett.*, vol. 19, no. 12, pp. 2082–2085, 2015.

[34] D. P. Bertsekas, *Nonlinear programming*. Athena Scientific Belmont, 1999.

Suraj Suman received the B.Tech. degree in Electronics and Communication Engineering from Indian Institute of Information Technology, Design and Manufacturing Jabalpur, India, in 2013, and the M.Tech. degree from Indian Institute of Technology Patna, India, in 2015. He is currently pursuing the Ph.D. degree in the Department of Electrical Engineering at Indian Institute of Technology Delhi, New Delhi, India. His current research interests include green communications, energy harvesting, and aerial communication system.

Swades De [S'02-M'04-SM'14] is a Professor in the Department of Electrical Engineering at IIT Delhi. Before moving to IIT Delhi in 2007, he was a Tenure-Track Assistant Professor of Electrical and Computer Engineering at the New Jersey Institute of Technology (2004-2007). He worked as an ERCIM post-doctoral researcher at ISTI-CNR, Pisa, Italy (2004), and has nearly five years of industry experience in India on telecom hardware and software development (1993-1997, 1999). His research interests are broadly in communication networks, with emphasis on performance modeling and analysis. Current directions include energy harvesting sensor networks, broadband wireless access and routing, cognitive/white-space access networks, smart grid networks, and IoT communications. Dr. De currently serves as an Area Editor for the IEEE COMMUNICATIONS LETTERS and Elsevier Computer Communications, and an Associate Editor for the IEEE TRANSACTIONS ON VEHICULAR TECHNOLOGY, the IEEE WIRELESS COMMUNICATIONS LETTERS, and the IEEE NETWORKING LETTERS.